Direct observation of impact propagation and absorption in dense colloidal monolayers

Ivo Buttinoni[a,1,2], Jinwoong Cha[b,c,2], Wei-Hsun Lin[b,2], Stéphane Job[d,2], Chiara Daraio[c,3], and Lucio Isa[a,3]

[a]Laboratory for Interfaces, Soft Matter and Assembly, Department of Materials, ETH Zurich, 8093 Zurich, Switzerland; [b]Department of Mechanical and Process Engineering, ETH Zurich, 8092 Zurich, Switzerland; [c]Engineering and Applied Science, California Institute of Technology, Pasadena, CA 91125; and [d]Laboratoire Quartz, Unité de Recherche EA-7393, Institut Supérieur de Mécanique de Paris - Supméca, 93400 Saint-Ouen, France

Edited by David A. Weitz, Harvard University, Cambridge, MA, and approved October 3, 2017 (received for review July 10, 2017)

Dense colloidal suspensions can propagate and absorb large mechanical stresses, including impacts and shocks. The wave transport stems from the delicate interplay between the spatial arrangement of the structural units and solvent-mediated effects. For dynamic microscopic systems, elastic deformations of the colloids are usually disregarded due to the damping imposed by the surrounding fluid. Here, we study the propagation of localized mechanical pulses in aqueous monolayers of micron-sized particles of controlled microstructure. We generate extreme localized deformation rates by exciting a target particle via pulsed-laser ablation. In crystalline monolayers, stress propagation fronts take place, where fast-moving particles (*V* approximately a few meters per second) are aligned along the symmetry axes of the lattice. Conversely, more viscous solvents and disordered structures lead to faster and isotropic energy absorption. Our results demonstrate the accessibility of a regime where elastic collisions also become relevant for suspensions of microscopic particles, behaving as "billiard balls" in a liquid, in analogy with regular packings of macroscopic spheres. We furthermore quantify the scattering of an impact as a function of the local structural disorder.

colloidal crystals | wave propagation | impact absorption | elastohydrodynamics | laser ablation

The mechanisms of propagation and absorption of large stresses in particulate materials can be very different depending on the size of the particles and their arrangement. For regular packings of macroscopic spheres, e.g., in a Newton's cradle, stress pulses, including impacts and shocks, are conveyed through elastic contacts (Hertzian interactions) (1–3). This makes it possible to direct and focus them, if the material provides specific paths [e.g., linear chains (4, 5) or lattices (6)] for the stress propagation (7, 8). The presence of a dispersing fluid does not alter this physics, provided that two neighboring grains/particles gain enough relative inertia to perform elastic scattering, mediated by hydrodynamic interactions (9–11).

Instead, dense disordered packings of macroscopic grains are materials whose energy absorption is controlled by local structural rearrangements and dissipation (12, 13). Absence of inertia in dense suspensions of microparticles and nanoparticles typically prevents elastic collisions and provides similar routes for energy dissipation (14–17). At high Peclét numbers, shear dominates the structural response of the material and Brownian diffusion becomes negligible. For example, at sufficiently high strain rates (up to $\dot{\gamma} \approx 10^3$ s^{-1}) and volume fractions, shear establishes highly dissipative particle chains, where lubrication films break down and the response is dominated by frictional contacts (18–21), leading to a viscosity increase (discontinuous shear thickening). Additionally, during impacts, "snow-plough" jammed fronts of nondeformable spheres propagate through the material and efficiently absorb energy (14, 22, 23).

Here, we investigate the mechanism of localized stress propagation in 2D crystalline lattices and disordered ensembles of microparticles in a liquid. Using pulsed laser ablation (PLA) to excite localized mechanical pulses (24), we access a regime of extremely high local shear rates, sufficient to induce interparticle Hertzian contacts and therefore a response analogous to the one of regular and disordered collections of macroscopic spheres. We study the effects of fluid viscosity and microstructural order on the stress propagation at the single-particle level.

Colloidal monolayers are prepared using a suspension of light-absorbing (SiO_2 half-covered with 50 nm of gold) and light-transparent (SiO_2) particles (radius $R = 3.69$ μm) that sediment toward the bottom glass surface of an observation cell (*SI Materials and Methods* and Fig. 1*A*). The coated particles function as "shock initiators" (SIs). When a metallic surface is illuminated by pulsed laser light, heat is not dissipated quickly enough, and some material is ablated from the surface. The expansion of high-pressure plasma generates an isotropic pressure wave (Movie S1) that travels away from the ablated material (25, 26). SIs that are confined and have the axis that links the Au-coated and the uncoated hemispheres oriented perpendicular to the substrate (Fig. 1*A*) behave in the same fashion. Under illumination with pulsed laser light [laser energy (LE) 0.09 μJ < LE < 0.25 μJ, $\lambda = 532$ nm, pulse duration $t_{\text{pulse}} = 4$ ns, radius of the laser spot $\approx 3R$], the ablation of the gold coating triggers an ultrashort ($f = 1/2\pi t_{\text{pulse}} = 40$ MHz) pressure wave. This effect is illustrated in Fig. 1*B*. Upon PLA of the gold cap, the SI does not move, but a radial pressure wave develops and pushes the surrounding particles outward (red arrows). At radial distances

Significance

Single-particle characterization of the impact response has unveiled design principles to focus and control stress propagation in macroscopic granular crystalline arrays. We demonstrate that similar principles apply to aqueous monolayers of microparticles excited by localized mechanical pulses. By inducing extreme local deformation rates and tracking the motion of each particle with velocities that reach up to few meters per second, we reveal that a regime of elastic collisions, typically forbidden due to overdamping, becomes accessible. This provides insights on the stress propagation and energy absorption of dense suspensions upon fast deformation rates.

Author contributions: I.B., C.D., and L.I. designed research; I.B., J.C., W.-H.L., and S.J. performed research; I.B., J.C., W.-H.L., S.J., and L.I. analyzed data; and I.B., J.C., S.J., C.D., and L.I. wrote the paper.

The authors declare no conflict of interest.

This article is a PNAS Direct Submission.

[1]Present address: Physical and Theoretical Chemistry Laboratory, Department of Chemistry, University of Oxford, Oxford, OX1 3QZ, UK.

[2]I.B., J.C., W.-H.L., and S.J. contributed equally to this work.

[3]To whom correspondence may be addressed. Email: daraio@caltech.edu or lucio.isa@mat.ethz.ch.

This article contains supporting information online at www.pnas.org/lookup/suppl/doi:10.1073/pnas.1712266114/-/DCSupplemental.

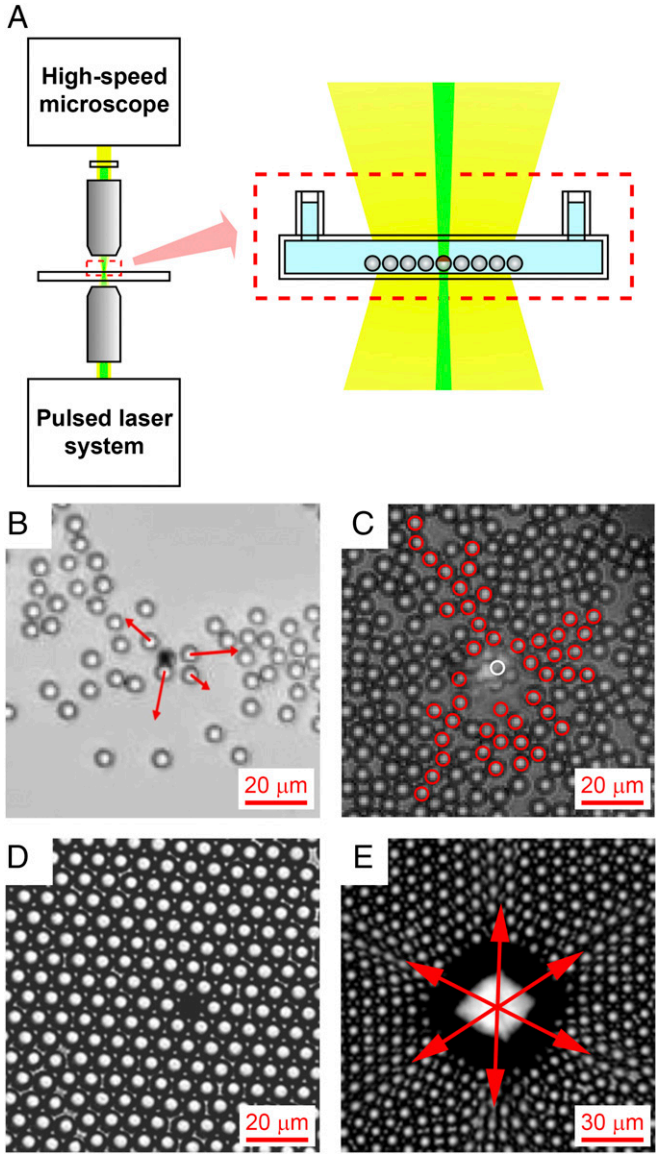

Fig. 1. Local excitation of colloidal monolayers via PLA. (*A*) Sketch of the experimental setup: Au-coated particles (SIs) on a glass surface are selectively excited by a green, pulsed laser beam and simultaneously imaged using a high-speed camera. (*B*) If the SI is sintered onto the substrate, the isotropic pressure wave generated by Au ablation sets into motion close-by particles and vanishes at larger distances. The arrows mark the particle displacements: The longest arrow denotes a displacement of 1.9 μm, and the others are drawn to scale (the arrows are magnified by a factor 8 for clarity). Particles with no arrow do not move. (*C*) Displacements farther away from the SI (white circle) occur only through interactions between particles aligned in chains. The red circles mark the moving particles. (*D*) Optical image of a colloidal lattice including one SI surrounded by uncoated beads. (*E*) High-speed frame after excitation, showing the preferential stress propagation along the symmetry axes of the crystal (red arrows; see also Movie S2).

larger than a few particle diameters, no motion is observed, suggesting that the pressure wave, and consequently the particle velocities, have decayed to zero. Despite this fact, in a semi-diluted monolayer (Fig. 1*C*), some particles that are located far away from the SI are also set into motion (red circles). Remarkably, the stress propagates only where the particles are close enough to contact and form chains. This observation rules out any possible long-distance displacement caused by the pressure wave or fluid flows associated to the ejected Au plasma, which are strictly isotropic (Fig. 1*B* and Movie S1). Particle–particle interactions are responsible for the propagation, instead. Further details on PLA are in *SI Materials and Methods*.

To study these interactions in well-defined structures, we assemble highly ordered (mean hexagonal order parameter $\psi_6 = 0.95 \pm 0.05$) 2D colloidal lattices of light-transparent particles (Fig. 1*D*, white particles) with a single light-absorbing inclusion (Fig. 1*D*, black particle). Under illumination of the SI by a laser pulse, the pressure wave sets into motion the first surrounding layer of particles. These particles travel radially due to inertia (Fig. 1*B*) and transmit the stress to the rest of the lattice (Movie S2). Here, the particles located along the symmetry axes of the monolayer move more efficiently than the others in the lattice (Fig. 1*E*, red arrows).

We monitor the propagation of strain through the colloidal crystals by recording images at ∼300 kHz and by measuring the global velocity V of the particles from their overall displacements (*SI Materials and Methods* and Fig. 2 *A*–*D*). We reach velocities up to few meters per second, far beyond the typical velocities of colloidal particles tracked in shear experiments (27–29). The laser pulse energy determines the initial velocity V_0 of the first layer of particles around the SI, as discussed below and in *SI Materials and Methods*. The lattice efficiently absorbs small stresses (e.g., Fig. 2*A*), whereas more intense perturbations propagate further in the crystals, traveling primarily along the symmetry axes (e.g., Fig. 2*D*). When the viscosity of the surrounding fluid is increased, at similar maximum propagation distances, the propagation becomes less directional, and all particles, including those not on the crystalline axes, undergo measurable displacements (compare Fig. 2*E*, $\eta = 1$ mPa·s and Fig. 2*F*, $\eta = 4$ mPa·s).

To understand the physics behind the propagation/absorption of local strains, we perform 2D numerical simulations of discrete particle lattices (*SI Materials and Methods*). We model the particles' motion accounting for Stokes' drag, Hertzian contacts (30), and hydrodynamic lubrication forces (31). We also set values for the average interparticle gap before excitation ($d = 400$ nm) and for the particle surface roughness ($\xi = 8.5$ nm) that match the experimental conditions (*SI Materials and Methods* and Fig. S1 *A* and *B*). We do not include contact friction between the particles. Friction between the particles and the substrate is also neglected, since a thin fluid film is always present and prevents direct contact (*SI Materials and Methods* and Fig. S1*C*). The simulations are initialized by setting the excitation velocity V_0. Numerical results for $\eta = 1$ mPa·s and $\eta = 4$ mPa·s (Fig. 2 *G* and *H*) faithfully reproduce the experiments shown in Fig. 2 *E* and *F* and reveal that the more isotropic propagation at large η stems from increasing lubrication forces, through which moving neighboring particles drag each other. The propagation depth of the strain waves into the colloidal lattice is estimated by studying the wave decay within the directions of maximum propagation, i.e., the symmetry axes around the SI. Numerical simulations allow the perturbation to be monitored by looking at the instantaneous particle velocities V_p (Fig. 2 *I* and *J*) along the alignment direction, from the excitation spot ($V_p = V_0$) to the periphery ($V_p \ll V_0$). The signature of interparticle contacts is revealed by a steep wavefront radiated from the SI, as long as the Hertzian elastic potential is involved in the interactions between the colloids (*SI Materials and Methods* and *SI Discussion*). The data confirms that larger fluid viscosity causes faster dissipation along symmetry axes. As soon as the momentum is too weak to lead to contact and elastic deformation, the steep front disappears in favor of a smoother decay (Fig. 2*J*, for $t > 0.2$ μs) driven by the diffusion of particle inertia, mediated by the fluid viscosity (*SI Materials and Methods* and *SI Discussion*). The speed of the steep wavefronts (Fig. 2*I*,

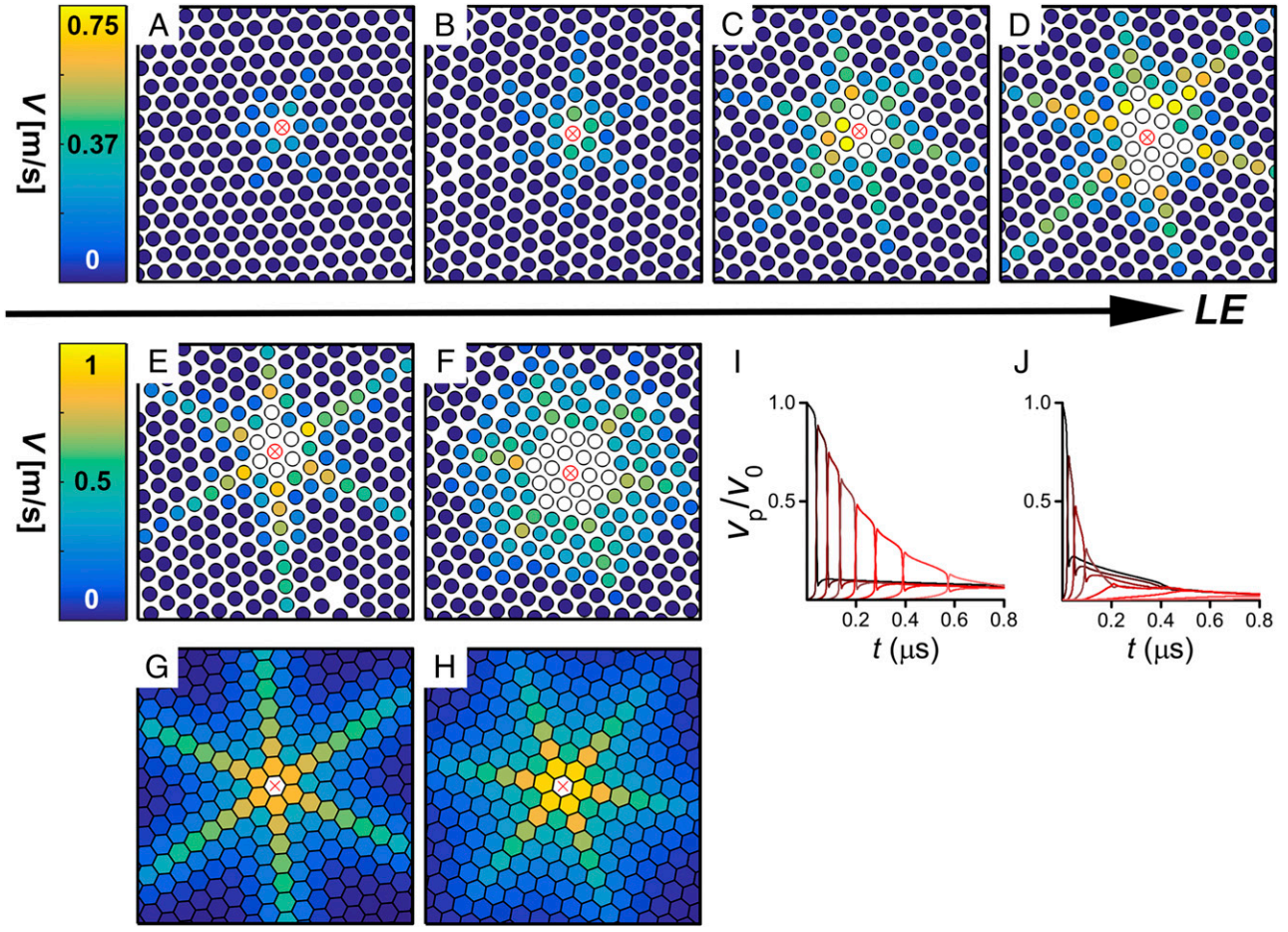

Fig. 2. Propagation of strain waves in 2D colloidal crystals at different excitation levels. (*A–D*) Experimental data in water (η = 1 mPa·s). The stress is transmitted along the six symmetry axes of the crystals. The global velocities *V* and the propagation distance increase with the laser pulse energy (LE). LE is (*A*) 0.09, (*B*) 0.14, (*C*) 0.15, and (*D*) 0.16 μJ. The red crosses correspond to the SIs. The surrounding white particles were not tracked because of their out-of-plane displacement (buckling). The size of the dots does not match the physical size of the particles. (*E* and *F*) In fluids with larger viscosity η, the stress propagation becomes more isotropic. LE is (*E*) 0.17 and (*F*) 0.25 μJ; η is (*E*) 1 and (*F*) 4 mPa·s. (*G* and *H*) Numerical simulations (drawn using Voronoi tessellation; see *SI Materials and Methods*) show the same behavior; η is (*G*) 1 and (*H*) 4 mPa·s. Excitation velocity V_0 is (*G*) 12 and (*H*) 26 m/s. (*I* and *J*) Decay of the instantaneous velocity V_p along a particle chain; η is (*I*) 1 and (*J*) 4 mPa·s. The colors correspond to different particles, from black (first particle next to the SI) to red.

$c_w \approx 165 \pm 25$ m/s and Fig. 2*J*, $c_w \approx 275 \pm 95$ m/s) is at least one order of magnitude larger than the velocity of the colloids and one order of magnitude smaller than the wave speed in the bulk material of the particles (c_0) or in the solvent (c_{water}), i.e., $V_0 \ll c_w \ll (c_0, c_{\text{water}})$. This distinct separation of timescales rules out any effect of flow advection or wave propagation in the fluid on the elastic wave radiation through the particle network. At these wave speeds, the wavelength $\lambda = c_w/f$ in the lattice is similar to the size of the particles and the size of the laser spot (~10 μm, *SI Materials and Methods*).

Experimentally, resolving the instantaneous particle velocity or the wavefront speed requires accuracy far beyond the capacity of high-speed optical imaging. Instead, the energy absorption properties and the full acoustic features (32) of the monolayers can be quantified from the decay of the global velocity *V* of the particles, and compared with the simulations. First, we fix the initial conditions, i.e., the LE in the experiments (Fig. 3 *A–C*, LE = 0.17 μJ) and the excitation velocity V_0 in the numerical simulations (Fig. 3 *D–F*, V_0 = 12 m/s), and then increase the viscosity of the medium (*SI Materials and Methods*). The quantitative agreement between simulations and experiments indirectly supports the hypothesis that the laser intensity determines the initial particle velocity. After excitation, the wave propagation is strongly affected by the solvent viscosity due to the fluid flow induced by the motion of the particles. This is further quantified by Fig. 3*G*, which shows how the global particle velocity decays along the symmetry axes of the crystal, i.e., along chains of particles *j* = 1, 2, ..., 6, as a function of their distance *L* from a given particle *i* with velocity V_i (*SI Materials and Methods*). A semilog plot of the data reveals an exponential decay $V_{j>i} = V_i \cdot \exp(-L/l_{\text{att}})$, where the attenuation length l_{att} measures the penetration depth of the mechanical perturbation. On average, l_{att} decreases with the viscosity of the dispersing fluid (Fig. 3*G*, *Inset*). Experiments (solid symbols) and simulations (empty symbols and solid line) reveal a similar response of the material to the applied pulse, in agreement with the velocity maps shown in Fig. 3 *A–F*. In the simulations, the attenuation length is robustly extracted from the decay of the energy field *E*, $\tilde{l}_{\text{att}}$, compatibly with the decay of the velocity field, $l_{\text{att}} = 2\tilde{l}_{\text{att}}$ [*SI Materials and Methods*: *E* is proportional to the kinetic energy of the particles, $E(r,t) \propto \exp(-r/\tilde{l}_{\text{att}}) \propto V^2(r) \propto \exp(-2r/l_{\text{att}})$, where *r* is the distance from the source].

The radial motion of the particles away from the SI is the consequence of two distinct mechanisms: (*i*) a radial expansion, driven by inertia and normal lubrication forces with diffusive

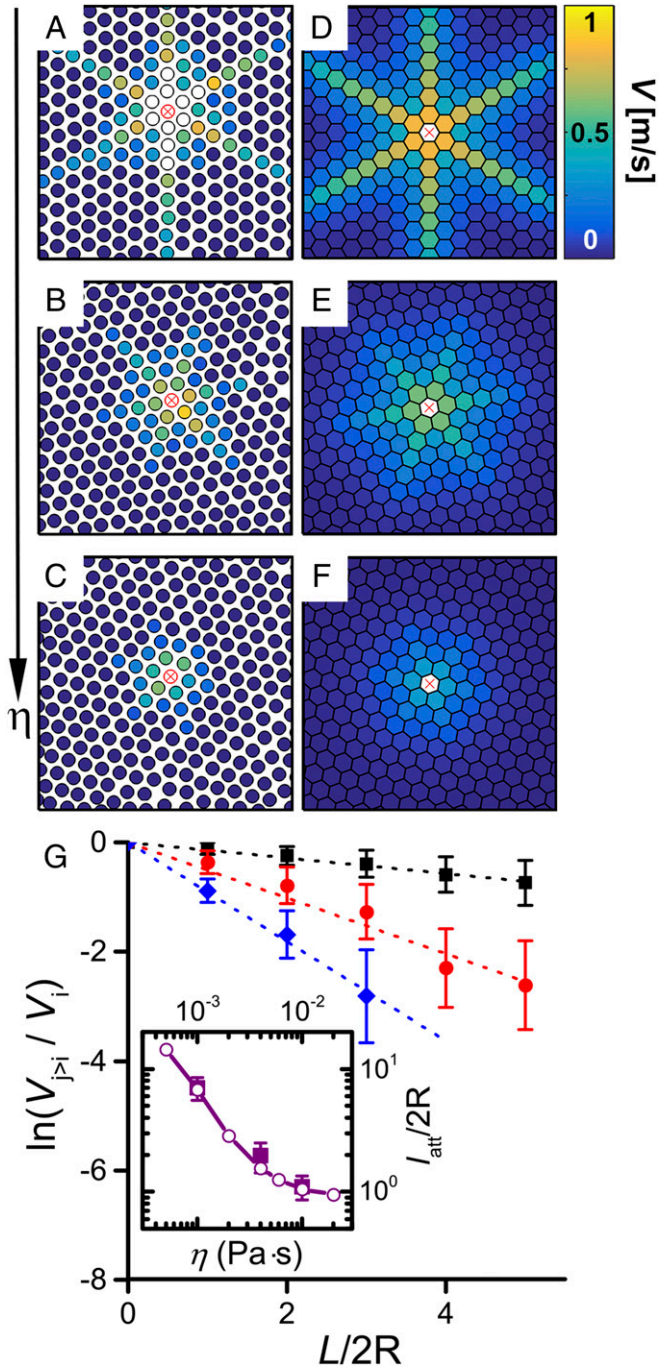

Fig. 3. Average strain wave penetration depth in 2D colloidal crystals dispersed in fluids with different viscosity. A fast dissipation in highly viscous fluids is revealed by the (*A*–*C*) experimental and (*D*–*F*) numerical velocity maps for η = (*A* and *D*) 1, (*B* and *E*) 4, and (*C* and *F*) 10 mPa·s. Initial conditions are fixed LE (experiments, LE = 0.17 μJ) and fixed instantaneous initial velocity (simulations, V_0 = 12 m/s). The average value of ψ_6, calculated over a circular region with a four-lattice-constants radius centered on the Sis, is (*A*–*C*) 0.98 ± 0.02 for the experiments and (*D*–*F*) 1 for the simulations. This dissipation is quantified by the (*G*) decay of the global velocity V for any initial velocity V_i of particles aligned along the symmetry axes of the crystal, plotted versus the distance from particle i (in units of 2R). Solid symbols correspond to experimental data obtained by averaging over ∼10 chains. Dashed lines are fits to the experimental data by an exponential law $V_{j>i} = V_i \cdot \exp(-L/l_{att})$ with a characteristic attenuation length l_{att}. The colors correspond to η = 1 (black), 4 (red), and 10 (blue) mPa·s. (*Inset*) Experimental (solid symbols) and numerical (empty symbols) attenuation lengths as a function of the viscosity of the dispersing medium. The solid line shows the trend of the numerical data.

momentum transfer and (*ii*) a weakly attenuated propagation, triggered by elastic deformations of the particles (9–11) (*SI Materials and Methods*). The first regime involves dissipation due to Stokes' drag and tangential lubrication interactions. In the second regime, when two colloids reach sufficiently small separation distances, the strain rate and the stress in the interstitial fluid diverge: the fluid clamped by its viscosity (11) within the surface roughness behaves in a "solid-like" manner (9, 33), and the particles deform elastically (strain > 10^{-4}) against the confined liquid layer. The particle surface roughness identifies the critical cutoff distance for occurrence of elastic deformation (9) (Fig. S1*A*). The behavior of l_{att} with η can be, in fact, only explained by taking into account elastic deformation of the particles, as captured by 2D numerical simulations (*SI Materials and Methods*) and compatibly with an elementary 1D description (*SI Discussion*). These conditions ($V \approx 1$ m/s, $\dot{\gamma}^{-1} \approx 10^{-6}$ s to 10^{-9} s) are in contrast to the case of jamming suspensions under shear flows (e.g., shear thickening $\dot{\gamma}^{-1} \approx 10^{-1}$ s to 10^{-3} s), in which the fluid has time to escape upon particle–particle contact (20, 21). These shear rates are also two to three orders of magnitude larger than macroscopic shear rates observed for impact protection materials employing shear-thickening fluid, but may become relevant for higher-energy projectiles, e.g., in spacecraft shielding (34).

The data presented were obtained using perfect hexagonal lattices. However, the stress propagation is drastically affected by particle misalignments (Fig. S3) and by the presence of structural defects in the lattices. We report the velocity maps of monolayers that include local defects, such as a dislocation (Fig. 4*A*) or a vacancy (Fig. 4*B*). In both cases, the stress propagation is abruptly arrested at the defect. In the extreme case of disordered (glassy) monolayers (*SI Materials and Methods* and Fig. 4*C*), the wave propagation becomes very short-ranged, even when the SI is illuminated at high power (LE = 0.16 μJ). Numerical simulations of aqueous monolayers (η = 1 mPa·s, V_0 = 12 m/s) with a controlled degree of disorder (*SI Materials and Methods*) highlight the propagation depth of stress pulses as a function of the hexagonal order parameter ψ_6 (Fig. 4*D*). The attenuation length $\tilde{l}_{att}$ of the ballistic coherent (35) field (*SI Materials and Methods*) swiftly drops to ∼2R, because of multiple scattering (35), within $0.85 < \psi_6 < 1$ (Fig. 4*D*, *Inset*, red), while the packing (area) fraction ϕ of the material remains constant (Fig. 4*D*, *Inset*, blue). This indicates that local order dictates the propagation of strain. Values of $\psi_6 < 0.85$ unavoidably lower the packing fraction and increase the initial separation d between the colloids (Fig. 4*E*). Fig. 4*F* shows the dependence of $\tilde{l}_{att}$ on d in disordered (any $\psi_6 < 1$, red) and crystalline ($\psi_6 = 1$, black) monolayers. In the crystalline case, $\tilde{l}_{att}$ depends weakly on d, whereas disordered structures cause stronger attenuations. This observation, in conjunction with Fig. 4*E* (ψ_6 vs. d), demonstrates that the decay of strain pulses in samples with randomness is due to multiple scattering rather than to the packing density.

All of our observations unambiguously show how the propagation of localized "extreme" strain waves depends on the excitation energy, the local particle arrangement, and the solvent viscosity. This mechanism is qualitatively different from direct (frictional) and indirect (hydrodynamic) contact-based models describing fluids jamming at lower shear rates. Instead, it sheds light on the mechanical response to much faster deformation rates, e.g., during impact and shocks, offering insights on the stress propagation and energy absorption of dense suspensions where elastic contacts can be specifically designed, e.g., by introducing local defects or by changing the solvent viscosity.

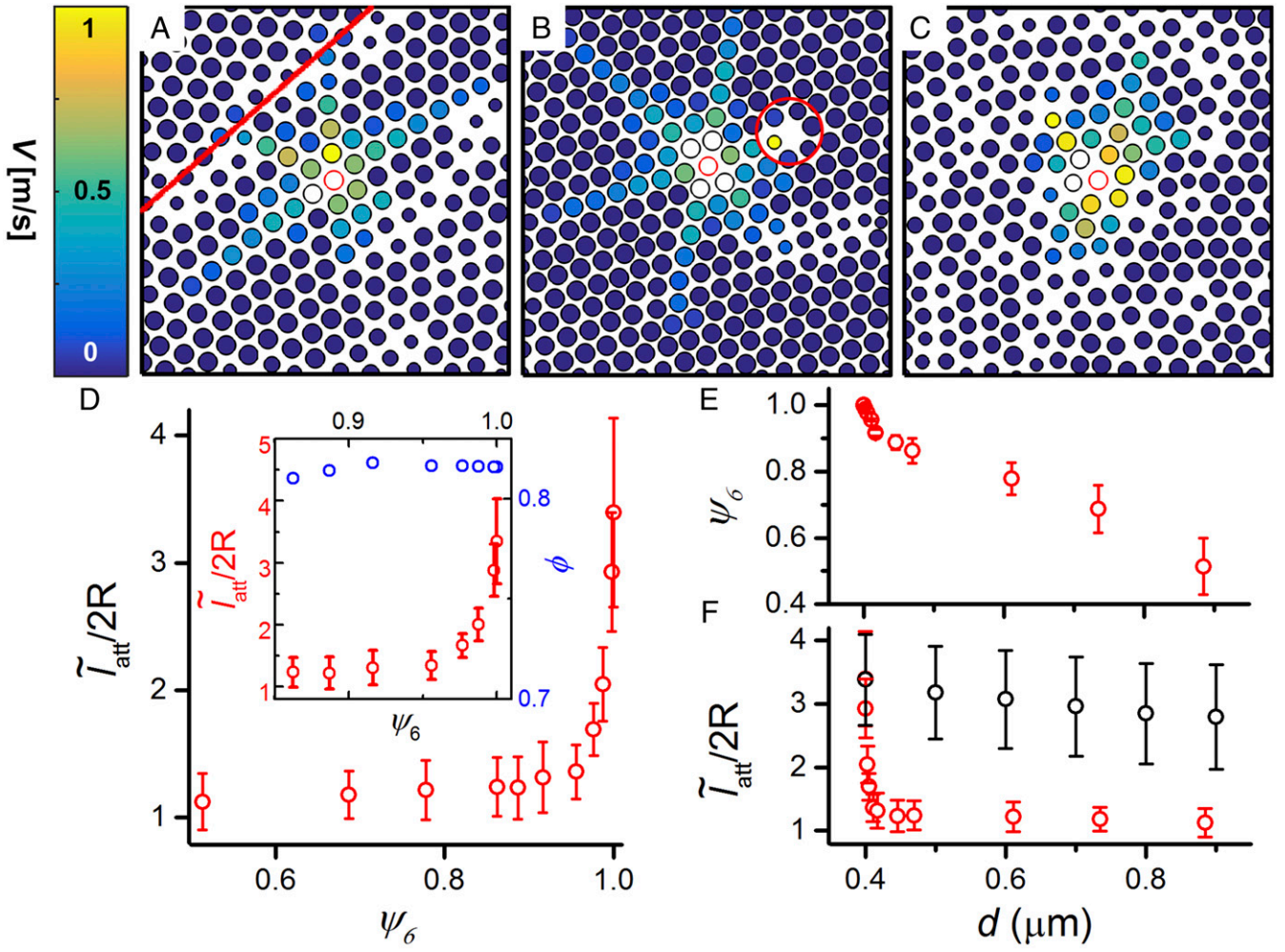

Fig. 4. Strain propagation in the presence of local disorder. (*A*–*C*) The pulse induced by the SI rapidly fades when traveling through (*A*) dislocations, (*B*) vacancies, or (*C*) glassy structures. The circles corresponding to particles are drawn with a size proportional to their value of ψ_6. (*D*) Attenuation length $\tilde{l}_{att}$ (in units of 2R, numerical data) extracted from the energy decay of the ballistic pulse (*SI Materials and Methods*) in colloidal monolayers excited in water at $V_0 = 12$ m/s. Each point is an average of 20 configurations. (*Inset*) At $0.85 < \psi_6 < 1$, the packing (area) fraction ϕ is constant (blue data) and $\tilde{l}_{att}$ shows a rapid decrease (red data); ϕ and ψ_6 are computed within a disk of radius 50 μm around the SI (i.e., the center of simulating box). (*E*) At $\psi_6 < 0.85$, the hexagonal order parameter ψ_6 and the initial mean interparticle distance d start to be strongly correlated. (*F*) Attenuation length $\tilde{l}_{att}$ as a function of d for a perfect crystal (black circles) and for disordered structures (red circles) prepared as described in *SI Materials and Methods*. The effect of the interparticle distance on $\tilde{l}_{att}$ is weak (black data), and the energy decay is mostly due to an increase of disorder.

ACKNOWLEDGMENTS. We thank Ramakrishna Shivaprakash Narve for the Atomic Force Microscopy friction and adhesion data and Michele Zanini and Svetoslav Anachov for particle roughness measurement and analysis. L.I. and I.B. acknowledge financial support from Swiss National Science Foundation Grant PP00P2_144646/1 and ETH Postdoctoral Fellowship FEL-02 14-1. S.J. acknowledges financial support from the Agence Nationale de la Recherche and the Fondation de Recherche pour l'Aéronautique et l'Espace, Project METAUDIBLE ANR-13-BS09-0003-01. C.D. acknowledges Air Force Office of Scientific Research Center of Excellence Grant FA9550-12-1-0091.

1. Porter MA, Kevrekidis PG, Daraio C (2015) Granular crystals: Nonlinear dynamics meets materials engineering. *Phys Today* 68:44–50.
2. Mueggenburg NW, Jaeger HM, Nagel SR (2002) Stress transmission through three-dimensional ordered granular arrays. *Phys Rev E Stat Nonlin Soft Matter Phys* 66: 031304.
3. Spannuth MJ, Mueggenburg NW, Jaeger HM, Nagel SR (2004) Stress transmission through three-dimensional granular crystals with stacking faults. *Granular Matter* 6: 215–219.
4. Carretero-González R, Khatri D, Porter MA, Kevrekidis PG, Daraio C (2009) Dissipative solitary waves in granular crystals. *Phys Rev Lett* 102:024102.
5. Job S, Melo F, Sokolow A, Sen S (2005) How Hertzian solitary waves interact with boundaries in a 1D granular medium. *Phys Rev Lett* 94:178002.
6. Leonard A, Daraio C (2012) Stress wave anisotropy in centered square highly nonlinear granular systems. *Phys Rev Lett* 108:214301.
7. Nesterenko V (2013) *Dynamics of Heterogeneous Materials* (Springer, New York).
8. Rosas A, Romero AH, Nesterenko VF, Lindenberg K (2007) Observation of two-wave structure in strongly nonlinear dissipative granular chains. *Phys Rev Lett* 98:164301.
9. Marshall J (2011) Viscous damping force during head-on collision of two spherical particles. *Phys Fluids* 23:013305.
10. Davis RH, Serayssol J-M, Hinch E (1986) The elastohydrodynamic collision of two spheres. *J Fluid Mech* 163:479–497.
11. Villey R, et al. (2013) Effect of surface elasticity on the rheology of nanometric liquids. *Phys Rev Lett* 111:215701.
12. Majmudar TS, Behringer RP (2005) Contact force measurements and stress-induced anisotropy in granular materials. *Nature* 435:1079–1082.
13. Clark AH, Petersen AJ, Kondic L, Behringer RP (2015) Nonlinear force propagation during granular impact. *Phys Rev Lett* 114:144502.
14. Waitukaitis SR, Jaeger HM (2012) Impact-activated solidification of dense suspensions via dynamic jamming fronts. *Nature* 487:205–209.
15. Lee YS, Wetzel ED, Wagner NJ (2003) The ballistic impact characteristics of Kevlar woven fabrics impregnated with a colloidal shear thickening fluid. *J Mater Sci* 38: 2825–2833.
16. Brown E, Jaeger HM (2014) Shear thickening in concentrated suspensions: Phenomenology, mechanisms and relations to jamming. *Rep Prog Phys* 77:046602.
17. Wagner NJ, Brady JF (2009) Shear thickening in colloidal dispersions. *Phys Today* 62: 27–32.
18. Wyart M, Cates ME (2014) Discontinuous shear thickening without inertia in dense non-Brownian suspensions. *Phys Rev Lett* 112:098302.

19. Royer JR, Blair DL, Hudson SD (2016) Rheological signature of frictional interactions in shear thickening suspensions. *Phys Rev Lett* 116:188301.
20. Fernandez N, et al. (2013) Microscopic mechanism for shear thickening of non-Brownian suspensions. *Phys Rev Lett* 111:108301.
21. Lin NY, et al. (2015) Hydrodynamic and contact contributions to continuous shear thickening in colloidal suspensions. *Phys Rev Lett* 115:228304.
22. Peters IR, Majumdar S, Jaeger HM (2016) Direct observation of dynamic shear jamming in dense suspensions. *Nature* 532:214–217.
23. Han E, Peters IR, Jaeger HM (2016) High-speed ultrasound imaging in dense suspensions reveals impact-activated solidification due to dynamic shear jamming. *Nat Commun* 7:12243.
24. Field J, Walley S, Proud W, Goldrein H, Siviour C (2004) Review of experimental techniques for high rate deformation and shock studies. *Int J Impact Eng* 30:725–775.
25. Phipps C, et al. (2010) Review: Laser-ablation propulsion. *J Propul Power* 26:609–637.
26. Bell C, Landt J (1967) Laser-induced high-pressure shock waves in water. *Appl Phys Lett* 10:46–48.
27. Chen DT, Wen Q, Janmey PA, Crocker JC, Yodh AG (2010) Rheology of soft materials. *Annu Rev Condens Matter Phys* 1:301–322.
28. Besseling R, Isa L, Weeks ER, Poon WC (2009) Quantitative imaging of colloidal flows. *Adv Colloid Interface Sci* 146:1–17.
29. Cheng X, McCoy JH, Israelachvili JN, Cohen I (2011) Imaging the microscopic structure of shear thinning and thickening colloidal suspensions. *Science* 333:1276–1279.
30. Johnson KL (1987) *Contact Mechanics* (Cambridge Univ Press, Cambridge, UK).
31. Jeffrey D, Onishi Y (1984) Calculation of the resistance and mobility functions for two unequal rigid spheres in low-Reynolds-number flow. *J Fluid Mech* 139:261–290.
32. O'Donnell M, Jaynes E, Miller J (1981) Kramers–Kronig relationship between ultrasonic attenuation and phase velocity. *J Acoust Soc Am* 69:696–701.
33. Barnocky G, Davis RH (1988) Elastohydrodynamic collision and rebound of spheres: Experimental verification. *Phys Fluids* 31:1324–1329.
34. Wagner N, Wetzel ED (2006) Conformable Ballistic Resistant and Protective Composite Materials Composed of Shear Thickening Fluids Reinforced by Short Fibers (Google Patents).
35. Page JH, Sheng P, Schriemer HP, Jones I (1996) Group velocity in strongly scattering media. *Science* 271:634–637.
36. Glycerine Producers' Association (1963) *Physical Properties of Glycerine and Its Solutions* (Glycerine Producers' Assoc, New York).
37. Chakrabarti J, Löwen H (1998) Effect of confinement on charge-stabilized colloidal suspensions between two charged plates. *Phys Rev E* 58:3400–3404.
38. Ni X, Rizzo P, Daraio C (2011) Laser-based excitation of nonlinear solitary waves in a chain of particles. *Phys Rev E Stat Nonlin Soft Matter Phys* 84:026601.
39. Kim S, Karrila SJ (2013) *Microhydrodynamics: Principles and Selected Applications* (Courier Corporation, North Chelmsford, MA).
40. Lee J-H, Gomez I, Meredith JC (2011) Non-DLVO silica interaction forces in NMP-water mixtures. I. A symmetric system. *Langmuir* 27:6897–6904.
41. Sen S, Hong J, Bang J, Avalos E, Doney R (2008) Solitary waves in the granular chain. *Phys Rep* 462:21–66.